Simulation of whispering gallery modes in the Mie regime using the nonstandard finite-difference time domain algorithm

Naoki Okada* and James B. Cole

Department of Computer Science, Graduate School of Systems and Information Engineering, University of Tsukuba, 1-1-1 Tennodai, Tsukuba, Ibaraki 305-8577, Japan
**Corresponding author: okada@cavelab.cs.tsukuba.ac.jp*

Received November 13, 2009; revised December 21, 2009; accepted December 25, 2009; posted January 7, 2010 (Doc. ID 119937); published March 3, 2010

The nonstandard (NS) finite-difference time domain (FDTD) algorithm has proved be remarkably accurate on a coarse numerical grid, but the well-known resonances called whispering gallery modes (WGMs) in the Mie regime are very sensitive to the scatterer representation on the computational grid, and a very large number of time steps are needed to correctly calculate the modes because the electromagnetic field outside the scatterer is weakly coupled to the inside. Using the NS-FDTD algorithm on a coarse grid, we were able to accurately simulate the WGMs of dielectric cylinders in the Mie regime. © 2010 Optical Society of America

OCIS codes: 260.5740, 290.4020.

1. INTRODUCTION

Whispering gallery modes (WGMs) were first observed as acoustic resonances in the interiors of such structures as cathedral domes and were analytically described by Lord Rayleigh [1]. Optical WGMs can be excited in dielectric and conducting objects. Debye [2] derived expressions for the resonance frequencies of dielectric and metallic spheres.

Since Garrett's [3] experimental work, WGMs have been used to measure spherical particle sizes, refractive index, and temperature [4]. In recent years much research effort has focused on microresonators, narrowband filters, optical switches, and biosensors using the properties of WGMs [5]. In addition WGMs have lately found various applications in optical communication and information processing.

For simple highly symmetric shapes such as infinite cylinders and spheres, Mie theory [6] can be used to calculate WGMs, but for more complicated shapes no general analytic solutions exist and numerical calculations are a necessity. The finite-difference time domain (FDTD) algorithm [7] can handle arbitrary shapes and has successfully been used to solve many problems. However the error of the conventional FDTD algorithm is proportional to $(h/\lambda)^2$, where h is the grid interval and λ is the wavelength and is large on a coarse grid. Recently we have derived a new version of the FDTD algorithm from a nonstandard (NS) finite-difference model [8] that gives much higher accuracy than the conventional FDTD. Although we had verified that NS-FDTD gives excellent results for off-resonance Mie scattering, we had not checked its accuracy for the WGMs in the Mie regime.

The electromagnetic fields of a Mie resonance are very sensitive to size, shape, and refractive index and vary rapidly with small perturbations. In FDTD calculations the result can be affected by perturbations of the algorithm parameters and by such extraneous parameters as how the scatterer is represented on the numerical grid and by how the computational domain is terminated. The correct calculation of WGMs in the Mie regime is thus a severe test of any numerical algorithm for optical modeling. We have used our NS-FDTD algorithm to compute the WGMs of infinite dielectric cylinders and have verified that we can achieve high accuracy on a relatively coarse numerical grid that is terminated with Berenger's perfectly matched layer (PML) absorbing boundary condition [9]. In this paper we give details of the algorithm and introduce improvements to our previously published algorithms.

2. WHISPERING GALLERY MODES

For simplicity, let us consider the two-dimensional Mie scattering problem in which an infinite plane wave of wavelength λ impinges upon an infinite dielectric circular cylinder parallel to the z axis of radius a and index of refraction n in the Mie regime $\lambda \sim a$ (Fig. 1). This problem can be separated into two modes: the transverse magnetic (TM) mode ($E_x=E_y=H_z=0$) and the transverse electric (TE) mode ($E_z=H_x=H_y=0$), where $\mathbf{E}=(E_x,E_y,E_z)$ is the electric field and $\mathbf{H}=(H_x,H_y,H_z)$ is the magnetic field. The geometry of the problem is illustrated in Fig. 1.

In the TM mode Maxwell's equations for $\mathbf{E}$ reduce to the Helmholtz equation in E_z,

$$(\nabla^2 + k^2)E_z = 0, \tag{1}$$

where $k=2\pi/\lambda$. In the TM mode the fields are independent of z, so $E_z=E_z(x,y)$. Outside the cylinder E_z is the

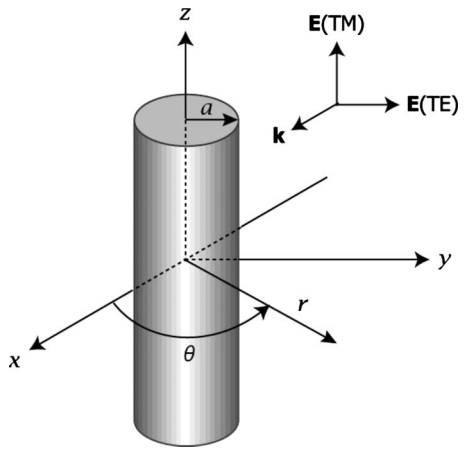

Fig. 1. Infinite plane wave impinging on an infinite dielectric cylinder (a=radius, $\mathbf{k}$=wave vector). TM and TE polarizations are shown. Wave propagates along the $+x$ axis.

sum of the incident field $E_z^0=e^{ikx}$, and the outgoing scattered field is E_z^s. Taking $(x,y)=r(\cos\theta,\sin\theta)$, $\mathbf{E}_z^s$ can be expanded in the form

$$E_z^s(r,\theta)=-\sum_{\ell=-\infty}^{\infty} i^\ell b_\ell H_\ell^{(1)}(kr)e^{i\ell\theta}, \tag{2}$$

where $H_\ell^{(1)}(x)$ is the Hankel function of the first kind and the b_ℓ are expansion coefficients to be determined. The electric field inside the cylinder, E_z^i, can be expanded in the form

$$E_z^i(r,\theta)=\sum_{\ell=-\infty}^{\infty} i^\ell d_\ell J_\ell(nkr)e^{i\ell\theta}, \tag{3}$$

where $J_\ell(x)$ is the Bessel function of the first kind, and the d_ℓ are expansion coefficients. The expansion coefficients in Eq. (2) and Eq. (3) are determined by the physical conditions that both E_z and its derivative normal to cylinder boundary $\partial_r E_z$ (∂_r means $\partial/\partial r$) must be continuous on the boundary. Using the fact that

$$E_z^0=e^{ikx}=\sum_{\ell=-\infty}^{\infty} i^\ell J_\ell(kr)e^{i\ell\theta}, \tag{4}$$

we obtain

$$E_z^i(r,\theta)=E_z^0(a,\theta)+E_z^s(a,\theta), \tag{5}$$

$$\partial_r E_z^i(r,\theta)=\partial_r E_z^0(a,\theta)+\partial_r E_z^s(a,\theta). \tag{6}$$

Using the identity $Z'_\ell(x)=Z_{\ell-1}(x)-(\ell/x)Z_\ell(x)$, where Z_ℓ stands for either J_ℓ or $H_\ell^{(1)}$, we can determine the expansion coefficients. Abbreviating $x=ka$, we find [6]

$$b_\ell(x,n)=\frac{nJ'_\ell(nx)J_\ell(x)-J_\ell(nx)J'_\ell(x)}{nJ'_\ell(nx)H_\ell^{(1)}(x)-J_\ell(nx)H'^{(1)}_\ell(x)}, \tag{7}$$

$$d_\ell(x,n)=\frac{J_\ell(x)-b_\ell(x)H_\ell^{(1)}(x)}{J_\ell(nx)}=\frac{J_{\ell-1}(x)H_\ell^{(1)}(x)-J_\ell(x)H_{\ell-1}^{(1)}(x)}{b_\ell^{\mathrm{d}}(x)}, \tag{8}$$

where b_ℓ^{d} denotes the denominator of b_ℓ.

Resonance occurs when the magnitude of one or more internal expansion coefficients becomes very large. From Eq. (8) we see that resonance occurs when b_ℓ^{d} is small, thus for $b_\ell^{\mathrm{d}}\to 0$ we obtain the condition

$$\frac{J_{\ell-1}(nka)}{J_\ell(nka)}=\frac{1}{n}\frac{H_{\ell-1}^{(1)}(ka)}{H_\ell^{(1)}(ka)}. \tag{9}$$

For example, at $x=ka=\pi$ and $n=2.745$, $|d_\ell|$ becomes large at $\ell=6$, whereas $0\leqslant|b_\ell|\leqslant 1$, as shown in Fig. 2.

For $ka=\pi$, b_ℓ^{d} vanishes at $n\cong 2.745-i1.506\times10^{-3}$, but this is nonphysical because it describes a material that is producing energy, not absorbing it. One might intuitively think that the resonance condition is given by $2\pi a=\ell n\lambda$, but this only holds when $a\gg\lambda$ (geometric optics), but not in the Mie regime. More example resonance conditions for the TM mode are given in Table 1a.

The TE mode can be analyzed in a similar way, and the resonance condition can be derived. It is given by

$$\frac{J_{\ell-2}(nka)}{J_{\ell-1}(nka)}=n\frac{H_{\ell-2}^{(1)}(ka)}{H_{\ell-1}^{(1)}(ka)}-\frac{(\ell-1)(n^2-1)}{nka}. \tag{10}$$

From Eq. (10), we find some example resonance conditions for the TE mode that are given in Table 1b.

A similar analysis can be carried out in three dimensions to find the spherical resonances.

3. FINITE-DIFFERENCE TIME DOMAIN ALGORITHMS

A. Standard FDTD Algorithm

The propagation and scattering of electromagnetic radiation is governed by Maxwell's equations. In nonconducting, dispersionless, linear isotropic media they can be expressed in the form

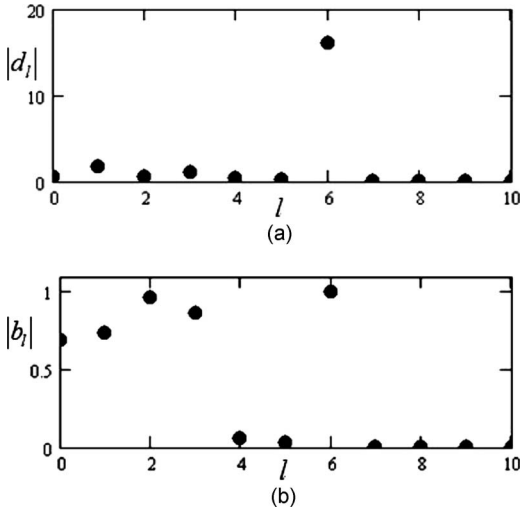

Fig. 2. Expansion coefficients for a resonance. Absolute values of (a) d_ℓ and (b) b_ℓ, respectively.

Table 1. Examples of Resonance Conditions for TM and TE Modes[a]

(a) TM Mode

Radius a	Refractive Index n	Mode Number ℓ
0.50 λ	2.745	6
0.75 λ	2.310	8
1.00 λ	2.717	10

(b) TE Mode

Radius a	Refractive Index n	Mode Number ℓ
0.50 λ	2.683	6
0.75 λ	2.529	9
1.00 λ	2.887	11

[a]λ = incident wavelength

$$-\mu\partial_t\mathbf{H} = \nabla\times\mathbf{E}, \tag{11}$$

$$\varepsilon\partial_t\mathbf{E} = \nabla\times\mathbf{H} - \mathbf{J}, \tag{12}$$

where the magnetic field $\mathbf{H}$ and the electric field $\mathbf{E}$ are functions of position $\mathbf{r}=(x,y,z)$ and time t. We assume that both magnetic permeability μ and electric permittivity ε are functions of $\mathbf{r}$ but not of t. $\mathbf{J}=\mathbf{J}(\mathbf{r},t)$ is a given external source current, and we also assume that the charge density vanishes everywhere, $\nabla\cdot(\varepsilon\mathbf{E})=0$). In free space without boundaries, Maxwell's equations reduce to the wave equation in each component and can be solved analytically, but when there are boundaries between different media there are no general analytic solutions. For example, in the Mie scattering problem discussed in the previous section, Maxwell's equations can be solved only for highly symmetric scatterers such as infinite cylinders, spheres, and certain infinitely periodic structures. In the case of more complicated boundaries, numerical methods must be used.

The FDTD algorithm is popular because it is easy to program and can handle arbitrary scatterer shapes, and it gives the time dependence of the electromagnetic fields. The FDTD algorithm is derived by replacing the derivatives in Maxwell's equations with central finite-difference (FD) approximations. The FD approximation to a derivative is given by

$$\frac{\mathrm{d}f(x)}{\mathrm{d}x} \cong \frac{d_x f(x)}{\Delta x}, \tag{13}$$

where d_x is a difference operator defined by $d_x f(x)=f(x+\Delta x/2)-f(x-\Delta x/2)$. For reasons that will soon be obvious we call Eq. (13) the standard (S) FD approximation. Analogously defining d_y, d_z, and d_t, we define the vector difference operator

$$\mathbf{d} = d_x\hat{\mathbf{x}} + d_y\hat{\mathbf{y}} + d_z\hat{\mathbf{z}}, \tag{14}$$

where $\hat{\mathbf{x}},\hat{\mathbf{y}},\hat{\mathbf{z}}$ are unit basis vectors in Cartesian coordinates.

Replacing the derivatives in Eq. (11) and Eq. (12) with the S-FD approximation, we obtain what we call the standard finite difference model,

$$d_t\mathbf{H}^t = \frac{\Delta t}{\mu h}\mathbf{d}\times\mathbf{E}^t, \tag{15}$$

$$d_t\mathbf{E}^{t+\Delta t/2} = \frac{\Delta t}{\varepsilon h}\mathbf{d}\times\mathbf{H}^{t+\Delta t/2} - \frac{\Delta t}{\varepsilon}\mathbf{J}^{t+\Delta t/2}, \tag{16}$$

where we write $\mathbf{H}(\mathbf{r},t)\to\mathbf{H}^t$ (similarly for $\mathbf{E}$ and $\mathbf{J}$) and have set $\Delta x=\Delta y=\Delta z=h$ (uniform numerical grid). In order to take central FDs with respect to time, $d_t\mathbf{H}$ is evaluated at t and $d_t\mathbf{E}$ at $t+\Delta t/2$. Although it is suppressed in the notation, each electromagnetic field component is located at a different point on the numerical grid. For example, in the TE mode (see Section 2) taking $E_x=E_x(x,y+h/2,t)$, $E_y=E_y(x+h/2,y,t)$, and $H_z=H_z(x,y,t+\Delta t/2)$, we can model Maxwell's equations with central FDs. Other choices are possible.

Expanding $d_t\mathbf{H}(\mathbf{r},t)$ and $d_t\mathbf{E}(\mathbf{r},t+\Delta t/2)$ and solving for $\mathbf{H}(\mathbf{r},t+\Delta t/2)$ and $\mathbf{E}(\mathbf{r},t+\Delta t)$ yields what we call the S-FDTD algorithm,

$$\mathbf{H}^{t+\Delta t/2} = \mathbf{H}^{t-\Delta t/2} - \frac{\Delta t}{\mu h}\mathbf{d}\times\mathbf{E}^t, \tag{17}$$

$$\mathbf{E}^{t+\Delta t} = \mathbf{E}^t + \frac{\Delta t}{\varepsilon h}\mathbf{d}\times\mathbf{H}^{t+\Delta t/2} - \frac{\Delta t}{\varepsilon}\mathbf{J}^{t+\Delta t/2}. \tag{18}$$

Given $\mathbf{H}(\mathbf{r},t-\Delta t/2)$ and $\mathbf{E}(\mathbf{r},0)$, all subsequent fields can be calculated. Notice that the FDTD algorithm does not explicitly include the boundary conditions at the media interfaces. So long as $\mathbf{H}(\mathbf{r},t-\Delta t/2)$ and $\mathbf{E}(\mathbf{r},0)$ satisfy all boundary conditions, then all subsequent electromagnetic fields calculated with the FDTD algorithm satisfy the boundary conditions. This is because the boundary conditions derive from Maxwell's equations.

If an initial electromagnetic field that satisfies the boundary conditions is not known, the initial fields can be set to zero and we can generate the incident field with the source term $\mathbf{J}$ by turning it on at $t=0$. Since a zero field satisfies the boundary conditions, the electromagnetic field generated by the source continues to satisfy them as it interacts with the scatterer.

In the general Mie scattering problem, we do not know an initial field that satisfies the boundary conditions, so the incident field must be generated by a source term. The total electromagnetic field $(\mathbf{H},\mathbf{E})$, can be decomposed into the sum of the incident field $(\mathbf{H}^0,\mathbf{E}^0)$ and the scattered field $(\mathbf{H}^s,\mathbf{E}^s)$. The incident field $(\mathbf{H}^0,\mathbf{E}^0)$ propagates as if there were no scatterer and thus satisfies

$$-\mu_0\partial_t\mathbf{H} = \nabla\times\mathbf{E}, \tag{19}$$

$$\varepsilon_0\partial_t\mathbf{E} = \nabla\times\mathbf{H}, \tag{20}$$

where $\mu=\mu_0$ and $\varepsilon=\varepsilon_0$ in the medium in which the scatterer is immersed. For simplicity let us assume that $\mu=\mu_0$ everywhere. Taking $\mathbf{J}=0$ and subtracting Eq. (19) from Eq. (11) and Eq. (20) from Eq. (12) yields Maxwell's equations for the scattered fields

$$-\mu_0\partial_t\mathbf{H}^s = \nabla\times\mathbf{E}^s, \tag{21}$$

$$\varepsilon\partial_t\mathbf{E}^s = \nabla\times\mathbf{H}^s - (\varepsilon-\varepsilon_0)\partial_t\mathbf{E}^0. \quad (22)$$

The last term on the right of Eq. (22) is an effective source current that gives rise to the incident field. In the Mie scattering problem the incident electric field is $\mathbf{E}^0 = \hat{\mathbf{p}}e^{i(\mathbf{k}\cdot\mathbf{r}-\omega t)}$, where $\hat{\mathbf{p}}$ is its polarization, $\mathbf{k}$ is the wavenumber vector, and ω is the angular frequency.

The FDTD calculation is initialized by $\mathbf{H}^s(\mathbf{r},t-\Delta t/2)=0$ and $\mathbf{E}^s(\mathbf{r},0)=0$. To compute real fields we take the source current to be

$$\mathbf{J}(\mathbf{r},t) = (\varepsilon-\varepsilon_0)\Theta(t)\Im[-i\omega\mathbf{E}^0(\mathbf{r},t)], \quad (23)$$

where $\Im$ means the imaginary part, and Θ is a pseudo step function that turns on the current gradually to suppress numerical transients. We define $\Theta(t\leqslant 0)=0$ and $\Theta(t\geqslant 0)=1$, with a gradual rise on the interval $0\leqslant t\leqslant\tau$ where τ is the "rise time." Usually τ is set equal to several wave periods, but the calculation is generally insensitive to both the value of τ and the exact form of Θ. In Eq. (23) we take the imaginary rather than the real part so that the time dependence is $\sin(\omega t)$, which vanishes at $t=0$.

We hope that after a "sufficient" number of time steps N, the FDTD calculation converges to a true scattered field. As we will see, the appropriate value of N is not always obvious at first sight.

Any numerical algorithm is potentially unstable. For the S-FDTD algorithm it can be shown that Δt and h must satisfy the Courant–Friedrichs–Lewy (CFL) condition [10],

$$\frac{\omega\Delta t}{kh} \leqslant \frac{1}{\sqrt{D}}, \quad (24)$$

where $k=|\mathbf{k}|$, and D is the number of spatial dimensions.

B. Nonstandard FDTD Algorithm

The error of the S-FD approximation Eq. (13) is defined by $\epsilon_S f(x)=(\partial_x-d_x/h)f(x)$ and $\epsilon_S\propto h^2$. The error can be improved by reducing the grid size, except in one dimension—the computational cost rises faster than the accuracy. For example, reducing the grid size to half, the error becomes

$$h\to\frac{h}{2}\Rightarrow\epsilon_S\to\frac{\epsilon_S}{4}. \quad (25)$$

On the other hand, in D dimensions the computational cost is $C_S\propto 1/(h^D\Delta t)$. Additionally, the time interval Δt is proportional to h because of the CFL condition. Thus the computational cost becomes

$$h\to\frac{h}{2}\Rightarrow C_S\to 2^{D+1}C_S. \quad (26)$$

One could try to reduce the error by using higher-order FD approximations, but this not only complicates the algorithm, a higher-order difference equation may also have unstable spurious solutions. Using what is called a nonstandard (NS) FD approximation [11], however, it is possible to greatly reduce the error of the FDTD algorithm without reducing the grid spacing or using higher-order FD approximations.

The NS-FD approximation in one dimension has the form

$$\frac{df(x)}{dx}\cong\frac{d_x f(x)}{s(\Delta x)}, \quad (27)$$

where $s(\Delta x)$ is a "correction function." With an appropriate choice it is sometimes possible to reduce the approximation error to zero. It might appear that the choice

$$s(\Delta x)=\frac{d_x f(x)}{f'(x)} \quad (28)$$

would yield an exact FD expression, but this choice is not always valid because the right side of Eq. (27) must converge to $f'(x)$ in the limit $\Delta x\to 0$. Thus, from the definition of a differential, $s(\Delta x)$ must satisfy

$$\lim_{\Delta x\to 0} s(\Delta x)=\Delta x. \quad (29)$$

Expanding $s(\Delta x)$ in a Taylor series,

$$s(\Delta x)=s(0)+\Delta x s'(0)+\cdots. \quad (30)$$

When Eq. (30) satisfies Eq. (29), $s(\Delta x)$ requires two conditions, which are $s(0)=0$ and $s'(0)=1$. For the plane wave $\varphi(x)=e^{\pm ikx}$, Eq. (28) is valid. Putting $s(\Delta x)=s(k,\Delta x)$ into Eq. (27) where

$$s(k,\Delta x)=\frac{2}{k}\sin\left(\frac{k\Delta x}{2}\right) \quad (31)$$

gives an exact FD expression for $\varphi'(x)$.

In two and three dimensions, however, there is no exact NS-FD expression for $\partial_x\varphi(\mathbf{r})$, where $\varphi(\mathbf{r})=e^{\pm i\mathbf{k}\cdot\mathbf{r}}$ and $\mathbf{k}=k(\cos\theta,\sin\theta)$. Away from media boundaries in every homogeneous region, Maxwell's equations (neglecting source currents) reduce to the wave equation

$$(\partial_t^2-c^2\nabla^2)\psi(\mathbf{r},t)=0, \quad (32)$$

where ψ is an electromagnetic field component and c is the velocity of the propagation in the medium. We therefore need a "high accuracy" NS-FD expression for $\nabla^2\varphi$. For reasons explained in [8] we construct a new vector difference operator $\mathbf{d}_0$ such that $(\mathbf{d}_0\cdot\mathbf{d})\varphi/s(k,h)^2$ is a high-accuracy approximation to $\nabla^2\varphi$. We have found that

$$\mathbf{d}_0=\mathbf{d}+\frac{1-\gamma}{4}\left(\hat{\mathbf{x}}d_x\left(d_y^2+d_z^2+\frac{\eta}{3}d_y^2d_z^2\right)+\hat{\mathbf{y}}d_y\left(d_x^2+d_z^2+\frac{\eta}{3}d_x^2d_z^2\right)+\hat{\mathbf{z}}d_z\left(d_x^2+d_y^2+\frac{\eta}{3}d_x^2d_y^2\right)\right), \quad (33)$$

where

$$\gamma=\frac{2}{3}-\frac{1}{90}(kh)^2-\cdots, \quad (34)$$

$$\eta=\frac{2}{5}+\left(\frac{1913}{50400}-\frac{5\sqrt{2}}{252}\right)(kh)^2+\cdots. \quad (35)$$

For simplicity let us evaluate the error of the S-FD and NS-FD approximations for $\nabla^2\varphi$ in two dimensions. The error of the S-FD approximation becomes

$$\epsilon_S = \frac{1}{\varphi}\left(\nabla^2 - \frac{(\mathbf{d}\cdot\mathbf{d})}{h^2}\right)\varphi \cong \frac{k^2(kh)^2}{12}\sin^2 2\theta. \tag{36}$$

The error of the NS-FD approximation is

$$\epsilon_{NS} = \frac{1}{\varphi}\left(\nabla^2 - \frac{(\mathbf{d}_0\cdot\mathbf{d})}{s(k,h)^2}\right)\varphi \cong \frac{k^2(kh)^6}{24192}\left(\sqrt{2} - 1 - \frac{\sin^2 2\theta}{2}\right)\sin^2 2\theta. \tag{37}$$

Thus in two dimensions ϵ_S is proportional to $(kh)^2$, whereas ϵ_{NS} is proportional to $(kh)^6$. There are similar expressions in three dimensions.

Let us now derive the NS-FDTD algorithm. In many problems μ is a constant with respect to position and we are more interested in the electric field than in the magnetic field. In this case it is convenient to replace $\mathbf{H}$ with $\mathbf{H}_\mu = \mu h\mathbf{H}/\Delta t$ in Eq. (17) and Eq. (18). In addition we replace $\mathbf{d}$ with $\mathbf{d}_0$ in Eq. (18) and obtain

$$\mathbf{H}_\mu^{t+\Delta t/2} = \mathbf{H}_\mu^{t-\Delta t/2} - \mathbf{d}\times\mathbf{E}^t, \tag{38}$$

$$\mathbf{E}^{t+\Delta t} = \mathbf{E}^t + \frac{u_0^2}{\tilde{\varepsilon}}\mathbf{d}_0\times\mathbf{H}_\mu^{t+\Delta t/2} - \frac{\Delta t}{\varepsilon}\mathbf{J}_{NS}^{t+\Delta t/2}, \tag{39}$$

where $u_0 = s(\omega,\Delta t)/s(k,h) = \sin(\omega\Delta t/2)/\sin(kh/2)$, and $\tilde{\varepsilon} = \sin^2(\sqrt{\varepsilon}kh/2)/\sin^2(kh/2)$. Notice that in the limits $h, \Delta t \to 0$, $u_0 \to c$ (c is the propagation velocity in the medium in which the scatterer is immersed) and $\tilde{\varepsilon} \to \varepsilon$.

Generalizing the derivation of the CFL condition, the stability condition for the D dimensional NS-FDTD algorithm becomes

$$\frac{\omega\Delta t}{kh} \leqslant \frac{2\sqrt{D}}{\pi}\arcsin\left(\sqrt{\frac{2}{M_D}}\sin\left(\frac{\pi}{2\sqrt{D}}\right)\right), \tag{40}$$

where M_D is given in [8]. The maximum values of $\omega\Delta t/kh$ from Eq. (24) and Eq. (40) are shown in Table 2 for the S-FDTD and NS-FDTD algorithms. But these values have been corrected from those given in [8] and are shown in Table 2.

Table 2 indicates that the NS-FDTD algorithm allows a somewhat larger time step over the S-FDTD algorithm as D grows. For each grid point, the computational cost of the NS-FDTD algorithm is somewhat larger than S-FDTD, but this larger cost is somewhat offset by a larger time step and by the fact that a coarser grid can be used.

Table 2. Maximum Values of $\omega\Delta t/kh$ for S-FDTD and NS-FDTD Algorithm Stability

Dimension D	S-FDTD	NS-FDTD
1	1.000	1.000
2	0.707	0.799
3	0.577	0.746

4. SCATTERER REPRESENTATION ON GRID

A high-accuracy FDTD algorithm alone does not always guarantee a high-accuracy result. Other errors enter into the total calculation from such factors such as how the computational boundaries are terminated and how the scatterers are modeled on the numerical grid. The error of the FDTD algorithm can be made very small and good absorbing boundary conditions are available [9,12], so the largest remaining source of error is the representation of the scatterer.

The simplest representation is the staircase model. In Fig. 3(a), a scatterer of permittivity ε_1 (gray area) is immersed in a medium of permittivity ε_2 (white area), thus $\varepsilon(\mathbf{r}) = \varepsilon_1$ if grid point $\mathbf{r}$ lies within the scatterer, and $\varepsilon(\mathbf{r}) = \varepsilon_2$ otherwise. Although visual appearance of the model does not necessarily correlate with accuracy in FDTD calculations, the staircase model obviously fails to preserve important symmetries of the shape as the center is shifted [Figs. 3(b) and 3(c)], and large errors are likely to arise.

A better model, called the "fuzzy model," can be derived from Ampére's law,

$$\int_C \mathbf{H}\cdot d\mathbf{s} = \int_S \varepsilon\partial_t\mathbf{E}\cdot d\mathbf{S}. \tag{41}$$

First let us consider the TM mode as shown in Fig. 4(a). Using Stoke's theorem, the left side of Eq. (41) becomes

$$\int_C \mathbf{H}\cdot d\mathbf{s} = \int_S (\nabla\times\mathbf{H})\cdot d\mathbf{S}. \tag{42}$$

If Δx and Δy are sufficiently small, $\mathbf{H}$ is essentially constant and can be removed from the integration to give $\Delta x\Delta y(\nabla\times\mathbf{H})_z$. Similarly $\partial_t\mathbf{E}$ can be removed from the integration on the right side of Eq. (41), and we obtain

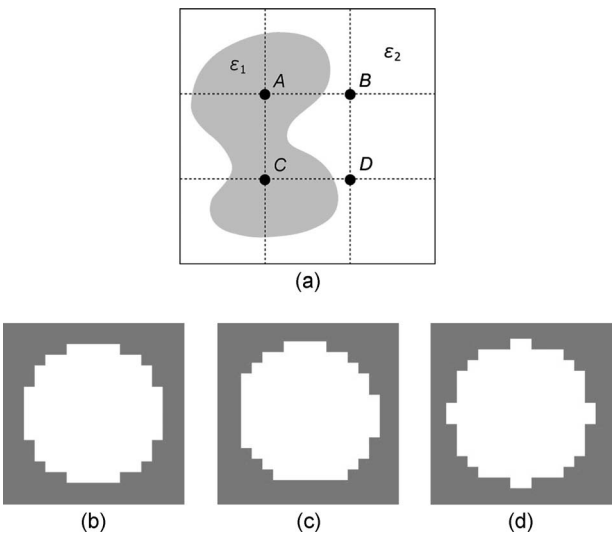

Fig. 3. (a) Staircase model. A and C are inside (gray), B and D are outside (white) the scatterer. (b)–(d) Circle of radius $6h$ (h = grid size) centered at $[(x+s)h,(y+s)h]$ (x,y are integers) for shift parameters $s = 0.0, 0.25, 0.5$ for (b), (c), (d), respectively.

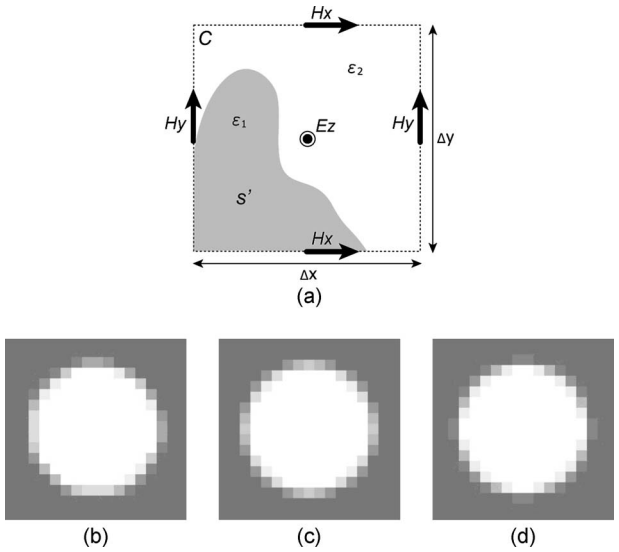

Fig. 4. (a) Integration of $\mathbf{H}$ on contour about E_z grid point. (b)–(d) Effect of shifting the center of a circle of radius $6h$. Center at $[(x+s)h,(y+s)h]$ (x,y are integers). $\Sigma_{x,y}\varepsilon(x,y)$ is invariant with respect to shifts $s=0.0$, 0.25, 0.5 for (b), (c), (d), respectively.

$$(\nabla \times \mathbf{H})_z \cong \langle \varepsilon \rangle_{xy} \partial_t E_z, \tag{43}$$

where $\int_S \varepsilon dx dy = \Delta x \Delta y \langle \varepsilon \rangle_{xy}$, and $\langle \varepsilon \rangle_{xy}$ means the average of ε about on the $x-y$ surface. For example, in Fig. 4, comparing the right sides of Eq. (41) with Eq. (43), we obtain

$$\langle \varepsilon \rangle_{xy} = \varepsilon_1 \left(\frac{S'}{\Delta x \Delta y} \right) + \varepsilon_2 \left(1 - \frac{S'}{\Delta x \Delta y} \right). \tag{44}$$

The fuzzy model assures a continuous range of values between ε_1 and ε_2 on the calculation grid rather than the binary values of the staircase model. Hence the symmetries are better preserved as the scatterer is shifted in Figs. 4(b)–4(d).

In the TE mode calculations, the fuzzy model can be derived by integrating E_x on the $y-z$ plane and E_y on the $x-z$ plane (Fig. 5). Because the electromagnetic fields are constant in the z direction, the permittivity ε is replaced by line averages. For example, we consider the Maxwell equation for E_x,

$$\varepsilon \partial_t E_x = \partial_y H_z. \tag{45}$$

As the grid point is (x,y), if E_x is positioned at $\mathbf{r}=(x,y+\Delta y/2)$ in the Yee algorithm [Fig. 5(a)], $\varepsilon(\mathbf{r})$ is replaced by,

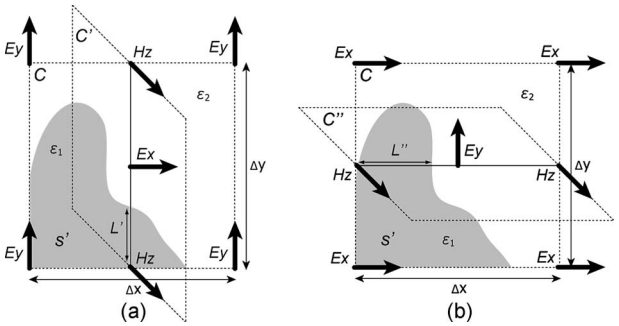

Fig. 5. Fuzzy model for the TE mode. Closed curves centered at (a) E_x and (b) E_y for Ampére's law.

$$\langle \varepsilon(\mathbf{r}) \rangle_y = \int_y^{y+\Delta y} \varepsilon(x,y) dy = \varepsilon_1 \left(\frac{L'}{\Delta y} \right) + \varepsilon_2 \left(1 - \frac{L'}{\Delta y} \right). \tag{46}$$

Similarly in the Maxwell equation for E_y at $\mathbf{r}=(x+\Delta x/2,y)$ [Fig. 5(b)], $\varepsilon(\mathbf{r})$ is replaced by $\langle \varepsilon(\mathbf{r}) \rangle_x = \int_x^{x+\Delta x} \varepsilon(x,y) dx$.

Although the fuzzy model improves the accuracy of FDTD calculations, it does not accurately represent features that are much smaller than the grid spacing. For example, in a dielectric of refractive index n the NS-FDTD algorithm empirically gives high accuracy for grid spacing $\Delta x=\Delta y=h \leqslant \lambda/(8n)$. But to compute accurately the transmission of a dielectric grating with a groove spacing of $\lambda/20$ (refractive index is n), we must set $h \leqslant \lambda/(20n)$. While it is possible to use finer sub-grids embedded in coarse ones to capture small features, Δt must be scaled down to satisfy the CFL stability condition for finer grids, and numerical instabilities also can arise at the interface between the coarse and fine grid. Some progress in model representation is discussed in [13].

5. SIMULATION OF WHISPERING GALLERY MODES

A. Transverse Magnetic Mode

We calculated the scattered field intensity at a resonance (WGMs) excited by an infinite plane wave impinging upon a dielectric cylinder in the TM mode (electric field parallel to the cylinder axis) and compared our results with the analytic solution of Mie theory. For example, using Eq. (9) we find that the $\ell=6$ resonance is excited in a cylinder of radius $a=0.5\lambda$ if the refractive index is set to $n=2.745$. We used both the S-FDTD and NS-FDTD algorithms and terminated the computational domain with a Berenger's PML using 16 layers. The scatterer was represented on the grid using the fuzzy model introduced in Section 4. We used the simulation parameters listed in Table 3. Since electromagnetic computations are scalable, to simulate infrared light ($\lambda=1280$ nm) impinging on a cylinder of radius $a=0.5\lambda=640$ nm we would take the grid interval to be $h=20$ nm, but the computational domain would still be 128×128 grid spacings (in other words, λ/h would remain unchanged).

Using the NS-FDTD and S-FDTD algorithms we compute the scattered field intensity $|E_z^s|^2$ and compare the results with Mie theory in Figs. 6(a)–6(c). In Fig. 6(d) we plot $|E_z^s|^2$ on a circular contour of radius $1.1a$ around the cylinder center and compare NS-FDTD and S-FDTD results with Mie theory. Intensity is visualized on a color scale ranging from blue (low) to red (high).

As is obvious in Fig. 6(d), the NS-FDTD algorithm is much more accurate than the S-FDTD algorithm. In this calculation, the discretization (ratio of wavelength to grid

Table 3. Computational Parameters of Whispering Gallery Mode Simulation in the Mie Regime

Grid Size	10 nm × 10 nm
Wavelength	640 nm
Cylinder radius	320 nm
Computation space	1280 nm × 1280 nm

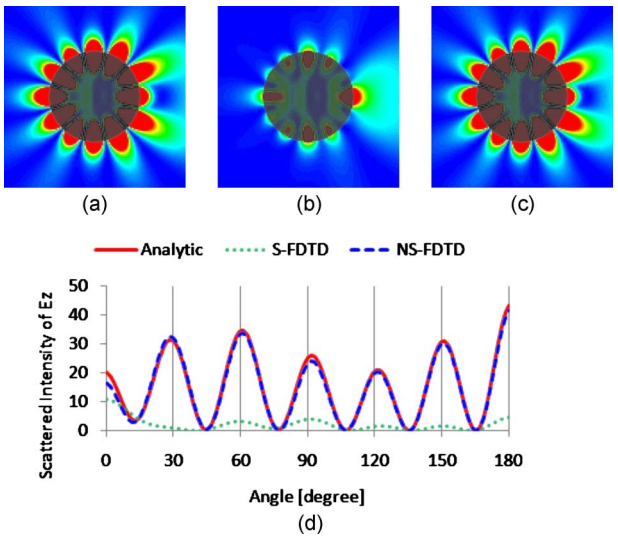

Fig. 6. (Color online) FDTD calculation of $|E_z^s|^2$ in the TM mode. (a) Analytic solution. (b), (c) Simulation results by S-FDTD and NS-FDTD algorithms at 100,000 time steps, respectively. (d) Angular intensity distributions.

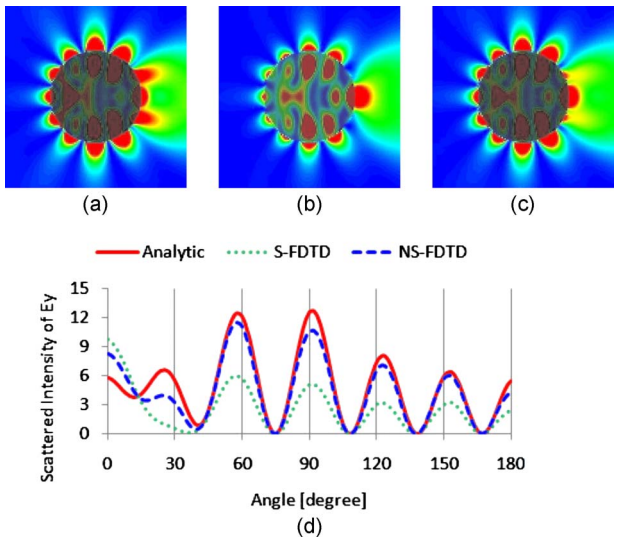

Fig. 7. (Color online) FDTD calculation of $|E_y^s|^2$ in the TE mode. (a) Analytic solution. (b), (c) Simulation results by S-FDTD and NS-FDTD algorithms at 100,000 time steps, respectively. (d) Angular intensity distributions.

interval inside the cylinder) is $\lambda/h=64$, which is necessary to get accurate results using the NS-FDTD algorithm. However, in off-resonance calculations, for example at $n=2.7$, the NS-FDTD algorithm gives highly accurate results only for $\lambda/h \geqslant 16$. We believe that this difference is due to errors in the scatterer model (shape representation) on the grid, because WGMs confine light to the cylinder and are sensitive to the shape, especially in the Mie regime.

B. Transverse Electric Mode

The calculation for the TE mode (electric field perpendicular to the cylinder axis) is similar to that of the TM mode, but now there are now two field components (E_x and E_y) located at different positions on the numerical grid. We chose the incident wave vector to be in the direction of the positive x axis, and the incident electric field to be polarized in the y direction. Since the E_x^s is relatively small, we examine the intensity of the scattered E_y field.

From Eq. (7), we find that the $\ell=6$ resonance mode is excited at $a=0.5\lambda$ and $n=2.683$. We computed the scattered field intensities using the S-FDTD and NS-FDTD algorithms and compared the results with Mie theory in Fig. 7. In the TE mode too, about 100,000 time steps are needed to obtain convergence.

As shown in Fig. 7, the NS-FDTD algorithm and the fuzzy model greatly improved the simulation accuracy. But although the accuracy to the NS-FDTD calculation is still far superior to the S-FDTD one, the accuracy of the FDTD calculation appears to be lower in the TE mode than in the TM mode. This is caused by the approximation of Gauss's law, which is given by

$$\mathbf{D}=\varepsilon\mathbf{E}, \quad \nabla\cdot\mathbf{D}=0 \tag{47}$$

for zero charge density. Using a vector identity, we obtain

$$\nabla\cdot(\varepsilon\mathbf{E})=\mathbf{E}\cdot\nabla\varepsilon+\varepsilon\nabla\cdot\mathbf{E}=0. \tag{48}$$

In the TM mode $\nabla\cdot\mathbf{D}=0\Rightarrow\mathbf{E}\cdot\nabla\varepsilon=\varepsilon\nabla\cdot\mathbf{E}=0$, because $\mathbf{E}$ is parallel to all media interfaces. In the TE mode however $\mathbf{E}=\mathbf{E}_\parallel+\mathbf{E}_\perp$, where $\mathbf{E}_\parallel$ is parallel to $\nabla\varepsilon$ and $\mathbf{E}_\perp$ is perpendicular to one. Thus $\nabla\cdot\mathbf{D}=0\Rightarrow\mathbf{E}_\parallel\cdot\nabla\varepsilon+\varepsilon\nabla\cdot(\mathbf{E}_\parallel+\mathbf{E}_\perp)=0$. This means that the direction of $\nabla\varepsilon$ matters in the TE mode but not in the TM mode. Thus, to improve the accuracy we must include information about $\nabla\varepsilon$ in the algorithm.

C. Convergence

For the calculation shown in Fig. 6, it took 100,000 time steps for the calculation to converge. At $\lambda=640$ nm 100,000 time steps correspond to about 0.24 [μs] in real time. This long convergence time is not just an artifact of the computational method, but is due to the fact that the electromagnetic field outside the cylinder is weakly coupled to the inside. The field energy density at resonance inside the cylinder is much larger than outside. Thus when the resonance is excited from outside the cylinder, the resonance takes a long time to build up. In our example, for $t/\Delta t \ll 100{,}000$, the scattered fields outside the cylinder are described very well by Eq. (2) with the $\ell=6$ mode excluded. On the other hand, off-resonance convergence is very rapid. In Fig. 8, using the parameters of Table 3 we compared the convergence for $n=2.745$ (resonance) and $n=2.7$ (off-resonance) for 1,000,000 time steps.

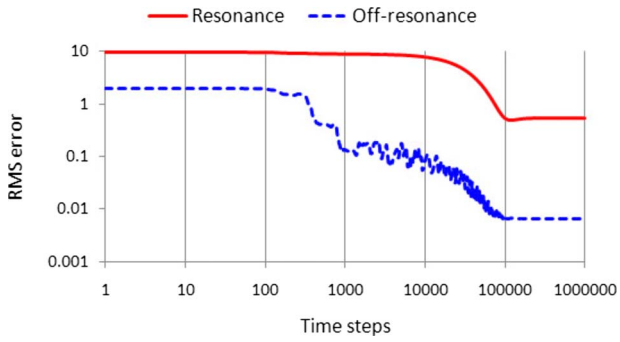

Fig. 8. (Color online) Convergence time for resonance and off-resonance modes. The ordinate is the rms error relative to Mie theory.

Figure 8 shows that the intensity in the FDTD resonance calculation rises so slowly that it seems to be constant over hundreds and even thousands of time steps. Thus if one does not realize that a resonance exists, one would be tempted to stop the calculation in the belief that it has converged. In this case we know the correct answer from Mie theory, but for irregular shapes for which no analytical solutions exist, the FDTD algorithm must be iterated for enough time steps to ensure true convergence.

Instead of exciting WGMs with an infinite plane wave impinging on the outside of the cylinder, they can also be excited by a point source inside the cylinder. In this case, the $\ell=6$ resonance develops after just a few thousand time steps [see Figs. 9(a)–9(c)]. In Fig. 9(d), we compare the rise of the WGM electric field intensity at the cylinder surface due to excitation by an external infinite plane wave and by an internal point source. As shown in Fig. 9(d), the surface intensity due to a point source builds up rapidly compared with plane wave excitations. But the point source must be placed where the intensity is high for the mode to be excited. In the example of Fig. 9, the source placed at $\mathbf{r}=(0,0.9a)$, but at the cylinder center it would not excite the $\ell=6$ resonance.

As seen in Fig. 6 and Fig. 7, the S-FDTD algorithm still has a large error even after 100,000 time steps. Finally, we investigated the root mean square (rms) error in the angular distribution of scattered intensity as a function of grid fineness for the S-FDTD and NS-FDTD algorithms in the WGM calculations. In the TM and TE resonance modes, we calculated the rms error relative to Mie theory at each λ/h as shown in Fig. 10. In Fig. 10(a), we see that the NS-FDTD result converges much faster than S-FDTD one in the TM mode, and we can estimate sensitivity of the shape (model representation) error for the S-FDTD and NS-FDTD algorithms. In FDTD calculations, the error consists mainly of algorithm error ϵ_A and shape error ϵ_S; absorbing boundary and round-off errors are ignored because they are relatively small. Thus the errors of the S-FDTD and NS-FDTD calculations are given by

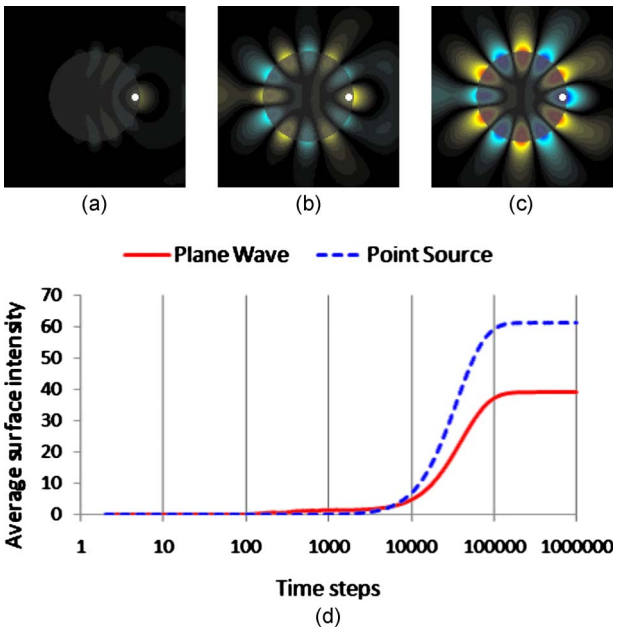

Fig. 9. (Color online) Whispering gallery mode excitation using a point source. (a)–(c) E_z^s on a color scale ranging from blue (minus) to red (plus), at 200, 1000, and 2000 time steps. The white dot is a point source. (d) Rise in surface intensity with the infinite plane wave and point source excitation.

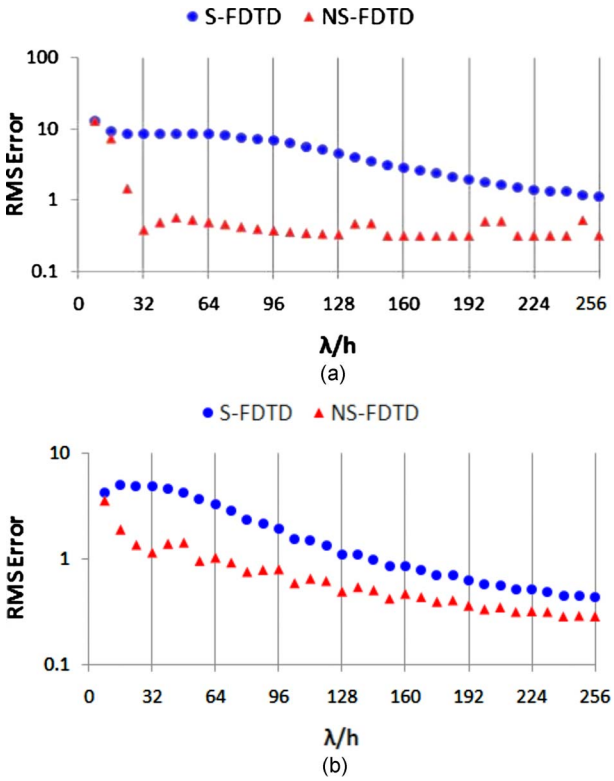

Fig. 10. (Color online) RMS error in the angular distribution of scattered intensity as a function of grid fineness (a) at 100,000 $\times(\lambda/h)/64$ time steps in the TM mode, (b) in the TE mode.

$$\epsilon^{S(\lambda/h)} \cong \tilde{\epsilon}_A^{S(\lambda/h)} + \tilde{\epsilon}_S^{S(\lambda/h)}, \tag{49}$$

$$\epsilon^{NS(\lambda/h)} \cong \tilde{\epsilon}_A^{NS(\lambda/h)} + \tilde{\epsilon}_S^{NS(\lambda/h)}. \tag{50}$$

In the TM mode at $\lambda/h=32$, $\tilde{\epsilon}_A^{NS(32)}$ is very small we can estimate the shape error of the NS-FDTD calculation to be

$$\tilde{\epsilon}_S^{NS(32)} \cong \epsilon^{NS(32)} \cong 0.384. \tag{51}$$

On the other hand the algorithm error of S-FDTD is proportional to $(h/\lambda)^2$ so $\tilde{\epsilon}_A^{S(32)}=\tilde{\epsilon}_A^{S(16)}/4$, and the maximum algorithm error at $\lambda/h=32$ is $\epsilon^{S(16)}/4$. Thus we estimate the minimum of shape error of the S-FDTD calculation to be

$$\min[\tilde{\epsilon}_S^{S(32)}] = \epsilon^{S(32)} - \frac{\epsilon^{S(16)}}{4} \cong 6.368. \tag{52}$$

Because $\tilde{\epsilon}_S^{NS(32)} \ll \min[\tilde{\epsilon}_S^{S(32)}]$, we conclude the shape error for the NS-FDTD algorithm is smaller than that of the S-FDTD one. In the TE mode [Fig. 10(b)], because they use different computational molecules the S-FDTD and NS-FDTD algorithms handle information about $\nabla\varepsilon$ differently, as discussed in Section 5.B. So the shape errors are likely to be different in the TE mode.

6. DISCUSSION AND CONCLUSIONS

We have demonstrated that the NS-FDTD algorithm can accurately compute WGMs in the Mie regime, which is a severe test of its performance. Compared with off-resonances the number of time steps needed for the calculation to converge is very large, and the convergence is slow because the coupling from outside to inside is weak. For irregularly shaped scatterers, where there is no analytic solution with which to compare, it is advisable to run the FDTD calculation enough time steps to confirm convergence. Compared to the S-FDTD algorithm, the NS-FDTD algorithm gives superior accuracy.

We believe that the dominant source of error in WGM calculations is the representation of the scatterer shape on the numerical grid, and the NS-FDTD algorithm reduces it more than the S-FDTD one. To calculate the WGMs correctly, a finer grid is needed than for off-resonance. For example, in the TM mode for a cylinder of radius 0.5λ and refractive index $n=2.7$ (off-resonance in Fig. 8), the NS-FDTD algorithm is in excellent agreement with Mie theory using even a grid discretization of $\lambda/h=16$, and the calculation converges after 5,000 time steps. However, on resonance when $n=2.745$, we must set $\lambda/h=64$ to get the same accuracy, and the calculation takes more than 100,000 time steps to converge.

The TE mode seems to more sensitive to shape representation than the TM mode. Whereas in the TM mode **E** is parallel to the boundaries, in the TE mode **E** has components both perpendicular and tangential to the boundaries. Simply averaging ε does not take into account information about the direction of the boundary interfaces that matter more in the TE mode.

Of course accuracy can always be increased by using more grid points to represent the shape, but this increases computational cost. Using the graphics processing unit (GPU), FDTD calculations can be dramatically accelerated [14]. Ultimately, however, a more accurate scatterer model on a coarse grid is needed to extend the range and speed of FDTD calculations. We have empirically examined some promising modifications to the fuzzy model, but have yet to derive them analytically and demonstrate their generality.

ACKNOWLEDGMENTS

We thank Dr. Ogawa of Fujikura Corporation, and the Japanese Ministry of Education and Science for financial support of this work. We thank Prof. S. Dutta Gupta of University of Hyderabad for proposing this problem.

REFERENCES

1. L. Rayleigh, "The problem of the whispering gallery," Philos. Mag. **20**, 1001–1004 (1910).
2. P. Debye, "Der Lichtdruck auf Kugeln von Beliebigem Material," Ann. Phys. **30**, 57–136 (1909).
3. C. G. B. Garrett, W. Kaiser, and W. L. Bond, "Stimulated emission into optical whispering gallery modes of spheres," Phys. Rev. **124**, 1807–1809 (1961).
4. P. Chyek, V. Ramaswamy, A. Ashkin, and J. M. Dziedzic, "Simultaneous determination of refractive index and size of spherical dielectric particles from light scattering data," Appl. Opt. **22**, 2302–2307 (1983).
5. A. B. Matsko, A. A. Savchenkov, D. Strekalov, V. S. Ilchenko, and L. Maleki, "Review of applications of whispering gallery mode resonators in photonics and nonlinear optics," IPN Progress Report, 42–162 (2005).
6. P. W. Barber and S. C. Hill, *Light Scattering by Particles: Computational Methods* (World Scientific, 1989).
7. K. S. Yee, "Numerical solution of initial boundary value problems involving maxwell's equations in isotropic media," IEEE Trans. Antennas Propag. **14**, 302–307 (1966).
8. J. B. Cole, "High-accuracy Yee algorithm based on nonstandard finite differences: new developments and verifications," IEEE Trans. Antennas Propag. **50**, 1185–1191 (2002).
9. J. P. Berenger, "A perfectly matched layer for the absorption of electromagnetic waves," J. Comput. Phys. **114**, 185–200 (1994).
10. S. K. Godunov, *Difference Schemes: An Introduction to the Underlying Theory* (North-Holland, 1987).
11. R. E. Mickens, *Nonstandard Finite Difference Models of Differential Equation* (World Scientific, 1994).
12. J. B. Cole and D. Zhu, "Improved version of the second-order Mur absorbing boundary condition based on a nonstandard finite difference model," Appl. Comput. Electromagn. Soc. J. **24**(4) (2009).
13. A. Farjadpour, D. Roundy, A. Rodriguez, M. Ibanescu, P. Bermel, J. D. Joannopoulos, S. G. Johnson, and G. Burr, "Improving accuracy by subpixel smoothing in FDTD," Opt. Lett. **31**, 2972–2974 (2006).
14. S. E. Krakiwsky, L. E. Turner, and M. M. Okoniewski, "Acceleration of finite-difference time domain (FDTD) using graphics processor units (GPU)," in IEEE MTT-S International Microwave Symposium Digest (IEEE, 2004), Vol. 2, pp. 1033–1036.